Numerical simulations of odorant detection by biologically inspired sensor arrays

2012 Bioinspir. Biomim. 7 016001

(http://iopscience.iop.org/1748-3190/7/1/016001)

Bioinspir. Biomim. **7** (2012) 016001 (16pp) doi:10.1088/1748-3182/7/1/016001

Numerical simulations of odorant detection by biologically inspired sensor arrays

R Schuech[1], M T Stacey[1], M F Barad[2] and M A R Koehl[3]

[1] Department of Civil and Environmental Engineering, University of California Berkeley, CA, USA
[2] Environmental Fluid Mechanics Laboratory, Stanford University, CA, USA
[3] Department of Integrative Biology, University of California Berkeley, CA, USA

E-mail: rudis@berkeley.edu

Received 25 May 2011
Accepted for publication 24 October 2011
Published 8 December 2011
Online at stacks.iop.org/BB/7/016001

Abstract
The antennules of many marine crustaceans enable them to rapidly locate sources of odorant in turbulent environmental flows and may provide biological inspiration for engineered plume sampling systems. A substantial gap in knowledge concerns how the physical interaction between a sensing device and the chemical filaments forming a turbulent plume affects odorant detection and filters the information content of the plume. We modeled biological arrays of chemosensory hairs as infinite arrays of odorant flux-detecting cylinders and simulated the fluid flow around and odorant flux into the hair-like sensors as they intercepted a single odorant filament. As array geometry and sampling kinematics were varied, we quantified distortion of the flux time series relative to the spatial shape of the original odorant filament as well as flux metrics that may be important to both organisms and engineered systems attempting to measure plume structure and/or identify chemical composition. The most important predictor of signal distortion is the ratio of sensor diameter to odorant filament width. Achieving high peak properties (e.g. sharpness) of the flux time series and maximizing the total number of odorant molecules detected appear to be mutually exclusive design goals. Sensor arrays inspired specifically by the spiny lobster *Panulirus argus* and mantis shrimp *Gonodactylaceus falcatus* introduce little signal distortion but these species' neural systems may not be able to resolve plume structure at the level of individual filaments via temporal properties of the odorant flux. Current chemical sensors are similarly constrained. Our results suggest either that the spatial distribution of flux across the aesthetasc array is utilized by *P. argus* and *G. falcatus*, or that such high spatiotemporal resolution is unnecessary for effective plume tracking.

(Some figures in this article are in colour only in the electronic version)

1. Introduction

1.1. Background

Scalar transport between small (sub-millimeter scale) cylinders or arrays of cylinders and the surrounding fluid is important in the modeling of many phenomena in biology and engineering, such as filters (Rubenstein and Koehl 1977, Kirsch 2007), artificial kidneys and lungs (Chan *et al* 2006) and the hair-bearing appendages many animals use for environmental sensing (Koehl 1992). The work reported here is motivated by the use of small-scale arrays of cylindrical chemical sensors, in both engineered systems (i.e. artificial noses) and living organisms (i.e. olfactory antennules), to sense chemicals dispersed in the fluid environment.

Scalar quantities released into a typical environmental flow of air or water form spatially and temporally complex plumes. These turbulent plumes consist of concentrated

filamentous structures interspersed with clean fluid (Crimaldi and Koseff 2001, Webster *et al* 2003, Crimaldi and Koseff 2006). We focus on the physical design of odor-sensing antennae composed of hair-like chemical sensors, a design inspired by the olfactory antennules of marine crustaceans, in order to measure microscale chemical plume structure. Many of these olfactory antennules bear arrays of chemosensory hairs that might be used to measure the spatial details of odorant patches in the environment (Koehl *et al* 2001, Koehl 2006). However, using arrays of sensors to achieve this goal presents an apparent dilemma to both animals and robots: the size and spacing of sensors must be comparable to the spatial scale of the plume features of interest, but at small scales, the physical presence of the sensors distorts the surrounding plume due to viscous effects. Thus, our intent is to quantify how the physical filtering process of capturing odorant molecules from the ambient fluid filters the 'odorant landscape' (Moore and Crimaldi 2004) observed by a plume-sampling agent.

Measurements of turbulent aquatic chemical plumes in the laboratory and environment have correlated the fine-scale structure (e.g. properties of individual chemical filaments) of the plume at a point with relative source location (i.e. upstream and lateral distance) and type of source (e.g. continuous versus pulsed) (Moore and Atema 1991, Webster and Weissburg 2001, Crimaldi *et al* 2002, Keller and Weissburg 2004). Since many crustaceans track plumes too rapidly to rely on gradients of mean properties such as time-averaged concentration (Grasso and Basil 2002, Webster and Weissburg 2009), it has been suggested that their sensors must sample the instantaneous properties of an odorant plume (Atema 1985, Moore *et al* 1991, Weissburg and Zimmer-Faust 1993, Gomez *et al* 1994, Zimmer-Faust *et al* 1995, Koehl 2001b, 2006, Moore and Crimaldi 2004, Page *et al* 2011a, 2011b). Furthermore, many crustaceans 'sniff', i.e. take discrete samples of the ambient water, each time they flick an antennule. Flume experiments have shown that dye filaments in a turbulent plume can be captured within crustacean chemosensory hair arrays during a flick and retained there until the next flick (Koehl *et al* 2001, Mead *et al* 2003). However, which odorant filament properties (if any) are detected and utilized by an animal is an exceedingly difficult question to test via laboratory experiments because of the scale (tens of microns in diameter) of the chemosensory hairs.

Although arrays of sensing elements are often employed in the experimental design of artificial noses and tongues, it is typically in the context of using sensors with different chemical sensitivities in order to identify the sample, or discern odor quality. Indeed, such an ability is the contemporary definition of an 'electronic nose'. While determining odor quality is clearly very important (e.g. food engineering), only a few researchers have investigated using chemical sensor arrays to better characterize the detailed spatial structure of the plume, and additionally, discern properties of the source such as the location or type of release (Kikas *et al* 2001a, 2001b, Cantor *et al* 2008). For instance, Cantor *et al* (2008) showed experimentally that a group of sensors arrayed in space greatly increases the ability to characterize a modulated plume, such as that formed by a pulsed release or the wake of a nearby obstacle. It is unknown whether biological chemosensor arrays may be used in a similar fashion.

There is a vast body of engineering literature on flow around and scalar (usually heat) transport to cylinders and arrays of cylinders. However, most of these studies are focused on traditional engineering applications and are not very applicable to biological sensor arrays. Many investigate geometries inappropriate to biological antennae (e.g. arrays of very long or infinite extent in the streamwise direction (Tamada and Fujikawa 1959, Stanescu *et al* 1996, Yoo *et al* 2007)) and flow at moderate to high Reynolds number (Re) (e.g. Chatterjee *et al* (2009), Han *et al* (2010)), whereas biological olfactory hairs operate at Re's of 10^{-1}–1 (e.g. Loudon and Koehl (2000), Goldman and Patek (2002), Koehl (2004)). Other engineering studies often focus on physical processes that are not relevant to odorant detection such as conjugate heat transfer or buoyant effects (e.g. Wang and Georgiadis (1996), Lange *et al* (1998), Juncu (2008)). One exception is an analytical solution by Friedlander (1957) for scalar transport to a single sphere at low Re, which although in a steady state, is compared to our results in section 3.2. It should be noted that dynamically scaled physical models of olfactory appendages (e.g. Reidenbach *et al* (2008)) have also proven useful, but practical requirements dictate that only the flow, not odorant transport, can be studied this way due to difficulties in scaling up both fluid momentum and scalar transport simultaneously.

To understand the fluid dynamics of odorant capture by crustacean antennules or biologically inspired artificial noses with small (tens of microns in diameter) hair-like sensors, a basic knowledge of the physical processes near the chemosensory hairs must be developed. This study focuses on perhaps the simplest type of sensor array and plume structure possible: an infinite row of 2D cylinders in low-Re crossflow, sampling a single odorant filament. Using numerical methods, we examine odorant transport to the cylindrical flux-detecting sensors in an effort to describe how sampling performance is determined by array geometry and sampling kinematics (i.e. how fast the sensor array is moved through the ambient fluid). We have three main objectives that will help inform the design of biologically inspired chemical sensor arrays.

- Quantify the effects of sensor array geometry and plume sampling kinematics on distortion of the environmental odorant signal (section 3.1).
- Quantify the effects of sensor array geometry and plume sampling kinematics on odorant flux metrics likely to be relevant to a plume sampling agent (section 3.2).
- Apply these results to biological chemosensor arrays and discuss implications for bio-inspired designs (section 3.3).

1.2. Biological sensor arrays and flux metrics

Along one of the filaments of the antennules of many aquatic malacostracan crustaceans (e.g. crayfish, crabs, mantis shrimp, lobsters) are arrays of hair-like structures, the aesthetascs, that contain the dendrites of hundreds of olfactory neurons enclosed by a thin, permeable cuticle (Gleeson 1982, Spencer and Linberg 1986, Laverack 1988, Grunert and Ache 1988, Hallberg *et al* 1992, Atema 1995,

Mead and Weatherby 2002). Although there are many other chemosensory structures on these animals, the aesthetascs are the most well studied and play an important, though not crucial, role in olfaction-mediated behavior such as plume tracking (Grasso and Basil 2002, Keller *et al* 2003, Horner *et al* 2004). A great diversity of aesthetasc array morphologies has evolved: e.g. the mantis shrimp *Gonodactylaceus falcatus* has relatively few, sparsely spaced aesthetascs, blue crabs (*Callinectes sapidus*) have toothbrush-like dense tufts of flexible aesthetascs on short antennules, and the spiny lobster *Panulirus argus* has a complex zig-zag arrangement of aesthetascs on long antennules. In each case, the entire structure encompasses a range of length scales, from the supporting antennule (mm in diameter) to the individual aesthetascs (20 μm in diameter in *P. argus* (Goldman and Koehl 2001)). The 'no-slip' condition dictates that the fluid velocity is zero along the entire surface of the sensory appendage, and the resulting boundary layers are thick relative to the size of the sensory hairs at the low Re's at which the hairs operate (Koehl 1996). The flow between the aesthetascs is laminar and transport across streamlines occurs via molecular diffusion.

All of these aesthetasc arrays consist of a finite (though sometimes very large) number of sensory hairs. Thus, water can flow both between hairs of the array and around the array as a whole. Cheer and Koehl (1987b) have quantified this flow feature with 'leakiness', which is the ratio of the volume of fluid that flows between neighboring hairs in a unit of time to the volume of fluid that would flow through the same area if the hairs were not there. Equivalently, leakiness can be defined as the ratio of the average fluid velocity in the gap between neighboring hairs to the freestream velocity. Mathematical and physical models of flow through a variety of small-scale hair-bearing appendages have revealed that they often operate in a critical range of Re where leakiness is very sensitive to morphology and sampling kinematics (Cheer and Koehl 1987a, 1987b, Koehl 1995, 2001a, 2001b, Mead and Koehl 2000, Loudon and Koehl 2000). At the lower end of this Re range (Re 10^{-2}), the boundary layers around each hair are thick and overlapping, and the entire appendage behaves as a solid paddle of low leakiness. At the higher end (Re 1), the boundary layers are thinner and the appendage behaves like a leaky sieve. This transition in flow regimes can critically affect the functioning of an olfactory appendage because it determines odorant access into the spaces between sensory hairs of the array (Loudon and Koehl 2000, Koehl *et al* 2001, Stacey *et al* 2002, Mead *et al* 2003).

We modeled sensor arrays of infinite cross-stream extent; thus, all the fluid must flow between the hairs of an infinitely wide row (it is maximally leaky). However, we matched properties of the flow between hairs of our infinitely wide rows with flow between real crustacean aesthetascs (see section 2.5) in an effort to minimize errors inherent in an infinite array approximation to reality.

Crustaceans such as *P. argus*, *G. falcatus* and *C. sapidus* flick the aesthetasc-bearing branch of their antennules back and forth through the water. In addition to the effects of sweeping through and sampling a two-dimensional region of the plume (Crimaldi *et al* 2002), flicking also increases leakiness (Koehl 1992, 2001a, Mead and Koehl 2000, Reidenbach *et al* 2008) and facilitates odorant penetration into dense arrays of aesthetascs (Koehl *et al* 2001, Mead *et al* 2003, Koehl 2006). Furthermore, the movement is asymmetric: the faster downstroke or outstroke exhibits high leakiness while the slower return stroke and inter-flick pause exhibit low leakiness. This has the effect of replacing an old water sample with a new one and then holding the new sample within the chemosensory array, a process likened to sniffing in mammals (reviewed in Koehl (2006)). We modeled steady flow as a simplification of this behavior, focusing on the flow that occurs during mid-downstroke and mid-return, but discuss implications of our simple model on real sniffing behavior in section 3.3.3.

During an odorant sampling event (a flick of the antennule through an odorant plume, e.g. Koehl *et al* (2001)), odorant molecules are transported via advection to the vicinity of an aesthetasc, reach the aesthetasc surface via molecular diffusion through the concentration boundary layer (e.g. Moore *et al* (1991)), diffuse through the permeable cuticle into the lumen of the aesthetasc (e.g. Derby *et al* (1997)), and finally diffuse to and bind to receptor proteins on the outer dendritic segment of an olfactory neuron (e.g. Grunert and Ache (1988)). We assume that these neurons act as odorant flux detectors such that the rate of odorant molecule arrival to the receptors affects the signal that is output from the neuron, encoded as a series of action potentials or 'spikes' (Kaissling 1998, Rospars *et al* 2000). Thus, our principal interest is in the time-varying flux of odorant into an aesthetasc, integrated over the cylindrical aesthetasc surface. For simplicity, hereafter we refer to the surface-integrated quantity as the 'odorant flux'. Although it is possible that variations in flux over a single aesthetasc might be perceived by animals, this seems unlikely due to neural convergence and we do not investigate such variation here even though engineered sensors might not have such limitations.

Neurobiological research has linked certain aspects of the time course of odorant molecule arrival at crustacean olfactory appendages with the firing of action potentials. Such experiments often delivered controlled pulses of odor-laden water to intact antennules or exposed axons of olfactory neurons in devices called 'olfactometers' (Gomez and Atema 1994, 1996a, Michel and Ache 1994, Hatt and Ache 1996, Gomez and Atema 1996b, Zettler and Atema 1999, Gomez *et al* 1999). Increasing the concentration of odorant in a pulse increased the rate of neuron spiking and the number of spikes, and decreased the response latency (Gomez and Atema 1996b). If odorant arrival to aesthetascs is governed by advection and molecular diffusion (described by a linear partial differential equation), the odorant pulse concentration is proportional to the flux to the aesthetascs, all other things being equal. Hence, we take the peak odorant flux during a sampling event to be an important metric of the flux time series. Lobster olfactory neurons also increase their spiking frequency as the rate of increase of odorant concentration near the aesthetascs (and thus the onset slope of flux) is increased (Zettler and Atema 1999). We must note that the timescales in Zettler and Atema (1999) were longer than the actual timescales of flux that we observe in this work, and there is evidence that the onset slope

might not be especially useful for plume tracking (Webster *et al* 2001). However, we include the peak onset slope in our analysis as a simple, representative aspect of transient sensor response, since it may be useful for odor quality determination (see below), and because similar quantities have been used successfully in plume tracking robots (Ishida *et al* 2005). Lastly, the olfactory receptors of crustaceans might need to interact with a certain number of odorant molecules in order to fire, analogous to the visual system requiring a certain number of photons (Barlow 1958, Hood and Grover 1974), although to our knowledge evidence of this has not yet been found in crustacean olfaction (Gomez and Atema 1996b). We include time-integrated flux, or total flux, in our analysis in light of this possibility as well as the fact that engineered chemical sensors might be designed with such properties.

While the ability of biological or electronic noses to measure microscale plume structure is a debated topic, it is clear that both systems must discriminate among different chemical compounds to be of great practical use. In electronic noses as well as the olfactory neurons of several animal species, the time courses of the response signals can be partially determined by chemical species (through the chemical kinetics occurring on and/or within the sensors (Spors *et al* 2006, Nakamoto and Ishida 2008, Junek *et al* 2010, Su *et al* 2011)) in addition to the effects of fluid dynamics that we focus on in this work. Of particular note, mutant fruit flies with olfactory receptor neurons that express just one functional type of odorant receptor can still distinguish different odorants, presumably based on temporal response dynamics alone (DasGupta and Waddell 2008). Likewise, the utility of analyzing transient aspects of sensor response to help discriminate odors is gaining recognition among electronic nose and tongue researchers (Amrani *et al* 1997, Hines *et al* 1999, Nakamoto and Ishida 2008, del Valle 2010). Hence, temporal parameters such as those we investigate here for flux detectors (peak flux, peak onset slope, total flux) may be important for both plume tracking and identification of an odor plume's chemical composition.

2. Methods

2.1. Numerics

2.1.1. Overview. We used numerical simulations to model the flow of water (viscosity $\nu \approx 10^{-6}$ m^2 s^{-1}) around arrays of cylinders tens of microns in diameter, as well as the advection and diffusion of low molecular weight odorant molecules (molecular diffusivity $k_D \approx 10^{-9}$ m^2 s^{-1}) to the cylinders, during a plume sampling event. Although it is possible to numerically model an array of sensors moving through water containing an odorant plume, it is typically much simpler to model the equivalent problem of water containing an odorant plume moving past a stationary array of sensors. This allows the computational grid to remain fixed in time, and is the approach employed here.

The arrays consisted of an infinitely long row of 2D cylinders, with various diameters and gap spacings. The steady fluid flow field for such geometry is set by a Reynolds number (we use $Re_{U_G,G}$, based on average gap velocity U_G and gap length G) and the gap to diameter ratio G/D of the array; see section 2.5 for details of our parameter space. Besides simplifying the interpretation of flux results since there are no array edge effects, such simple geometry is also computationally easy because an infinite array of cylinders can be represented numerically with just one cylinder in the computational domain. Figure 1 illustrates the computational unit. By using appropriate boundary conditions, symmetry of the flow and odorant concentration fields on both sides is enforced, thus being equivalent to that in an array of infinite extent.

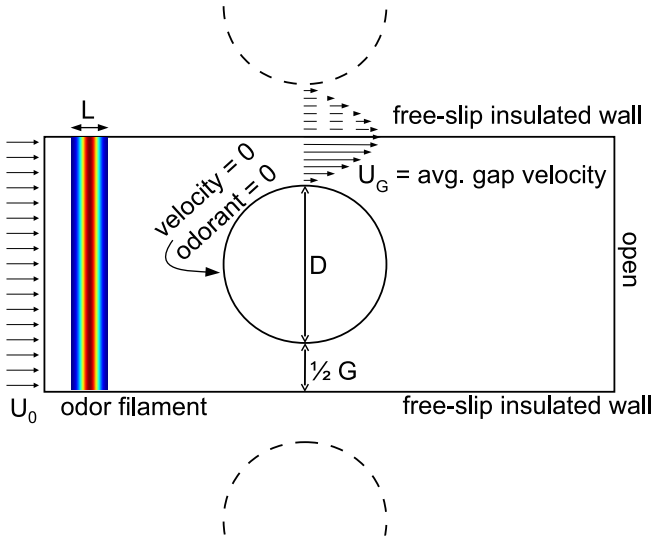

Figure 1. Schematic of geometry and boundary conditions. Items marked with dashed lines indicate neighboring subunits of the infinite array that are not explicitly modeled. The velocity profile in the gap is sketched. Domain length not to scale.

2.1.2. Boundary and initial conditions. At the inflow face of the computational domain (see figure 1), we use a Dirichlet condition for velocity, specifying a constant flow speed equal to the sampling speed of the array through the water. We use a time-varying Dirichlet condition for odorant concentration to advect a Gaussian-shaped odorant filament into the domain. We start with the ideal solution for a point mass M of odorant released at a point x_0 at time t_0 (far upstream of the computational domain) in an unbounded domain with uniform fluid velocity (i.e. sampling speed in the reference frame of the array) U_0 (Fischer *et al* 1979):

$$C(x,t) = \frac{M}{\sqrt{4\pi k_D (t-t_0)}} \exp\left\{ -\frac{[x - x_0 - U_0(t-t_0)]^2}{4k_D(t-t_0)} \right\}. \quad (1)$$

The parameters x_0, t_0 and M are determined by enforcing that for every simulation, the odorant filament has the same width L and peak concentration C_0 when its center reaches the leading edge of the cylinder in the case that it is undisturbed by the cylinder, i.e. equation (1). This standardizes the filaments

over the varying sampling velocities and domain sizes we used and accounts for diffusion of the filament before it reaches the array. The peak concentration of the filament was arbitrarily chosen to be $C_0 = 1$ mg L^{-1}, since the solution of the linear advection-diffusion equation will simply scale with this value, and the filament was chosen to be $L = 0.56$ mm wide (we assume 'width' to equal the smallest interval that contains 95% of the total odorant mass in the filament; this corresponds to a filament standard deviation $\sigma_{\text{filament}} = 0.14$ mm). This is in the same range as the 1 mm wide odor filaments used in a previous study of mantis shrimp odorant capture (Stacey *et al* 2002), although odorant patches in water as small as 0.2 mm have been measured (Moore *et al* 1992).

To reduce numerical errors associated with spatial and temporal discontinuities of concentration, we modify the odorant filament specified by equation (1) and replace the infinitely long tails with linear tails that drop off to exactly zero over a finite distance. This hybrid shape is determined by setting 99.9% of the mass in the odorant filament to be within the Gaussian core, and the remaining 0.1% to be in the linear tails. Thus, the resulting piecewise function varies from zero to linear to Gaussian from left to right toward the filament center; it is not explicitly given here. This 'Gaussian-linear' function is evaluated at the inflow domain face to specify the odorant concentration boundary condition over time. Although there is a slope discontinuity where the Gaussian core meets the linear tails, this appears to be insignificant in practice because both the concentration and slope are nearly zero at these locations.

The outflow face is 'open', with a viscous stress and stream-wise scalar gradient of zero imposed. Since this boundary condition forces gradients to be zero which may not be zero in a real unbounded domain, we carefully studied the effect of the proximity of the outflow face to the cylinder and ensured that enough downstream distance was present for the solution to develop properly (see section 2.3).

The side faces of the domain are slip walls: no flux of odorant or water is permitted through the wall, but velocity parallel to the wall is not constrained to be zero as would be the case with a real wall. Since there are planes of symmetry in the middle of every gap of an infinite array, the cross-stream gradient of any quantity along such planes is zero, as if there were slip walls present. Hence, the distance from the edge of the cylinder to the slip wall of our domain is equal to half the gap distance G of the infinite array we are modeling.

On the cylindrical sensor, we use a no-slip zero velocity condition for flow. This study focuses on the physical processes governing odorant molecule arrival at the aesthetasc surface, and consequently we idealize the processes thereafter. Thus, we employ a Dirichlet condition for odorant at the cylinder surface, and set the concentration to zero for all time. This results in a diffusive flux of odorant into the cylinder, which is recorded as the simulation progresses. This boundary condition models an ideal flux detector, which immediately and irrevocably consumes all odorant molecules that arrive on it, perhaps by rapid enzymatic degradation (Trapidorosenthal *et al* 1987, Carr *et al* 1990). We believe this to be a more appropriate model of olfactory sensors than the other straightforward alternative, a Neuman boundary condition, in which concentration would be measured instead of flux (Kaissling 1998, Rospars *et al* 2000).

The initial condition for velocity is computed as a potential flow solution, and the initial condition for concentration is zero everywhere, since initially the odorant filament is located far upstream of the computational domain. As the velocity field 'spins up' to the correct viscous, steady state field, the odorant filament hypothetically diffuses and advects toward the cylinder according to equation (1). The parameters of equation (1) and the final Gaussian-linear approximation are chosen such that the leading edge of the incoming linear tail of the odorant filament reaches the inflow face when the velocity field reaches the steady state. To determine an acceptable velocity steady state, we introduce a second, independent scalar specifically for this purpose. The boundary and initial conditions for this scalar are the same as for odorant, except that the inflow boundary condition is a constant concentration equal to 1 mg L^{-1}. Hence, this scalar advects into the empty domain as soon as the simulation begins, and eventually reaches the vicinity of the cylinder and begins to flux into it. When this flux stabilizes to two significant digits, the velocity field is assumed to be sufficiently steady and the odorant filament begins entering the domain. The convenience scalar is used since it allows a direct estimate of the effects of flow unsteadiness on the odorant flux.

2.1.3. Numerical method. The numerical method we use (Barad *et al* 2009) solves the incompressible Navier–Stokes equations for fluid motion and the scalar advection-diffusion equation for scalar transport. The method couples the embedded-boundary (or cut-cell) method for complex geometry with block-structured adaptive mesh refinement (AMR) while maintaining conservation and second-order accuracy. These features allow us to accurately resolve the scalar flux to the cylinders while using domains large enough to make boundary effects insignificant. For our simulations, AMR over time was not necessary, but local refinement around the cylinder was used to obtain accurate odorant fluxes (figure 2). To calculate the time-varying odorant flux into the embedded boundary of the cylinder, the finite-volume-based code computes a mass flow rate across the boundary for each Cartesian cell cut by the cylinder (see Barad *et al* (2009) for details), and then sums these contributions to obtain the spatially integrated flux into the cylinder, per unit length in the third dimension.

2.2. Sample output and shape parameters

2.2.1. Velocity field. Figure 3 shows a typical steady state velocity field. Note the relatively thick laminar boundary layer around the cylinder, and maximal velocities at the midpoints between cylinders (at the slip walls). The flow field is slightly asymmetric in the streamwise direction due to the non-negligible advective terms in the Navier–Stokes equations, which would be disregarded in a creeping flow regime. Since the array is of infinite extent, all flow is forced through the gaps and the peak speed in the gap in this case is about double the inflow velocity.

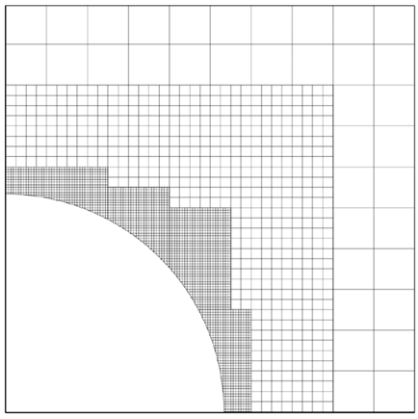

Figure 2. Section of a typical computational grid ($Re_{U_G,G} = 3$, $G/D = 2$) illustrating local refinement near the cylinder surface.

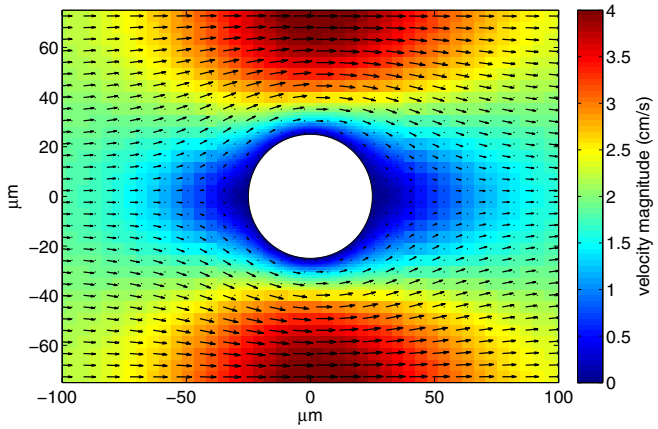

Figure 3. Velocity vector field and false-color rendering of velocity magnitude (speed) in the vicinity of a cylinder in the array for $Re_{U_G,G} = 3$, $G/D = 2$. No smoothing of the color rendering has been done to show the resolution of nested grids. Only a short streamwise section of the computational domain is shown for clarity.

Figure 4 summarizes velocity profiles of the streamwise velocity component within the gap for the parameter space we investigated. The flow speed is normalized by the inflow velocity U_0 and plotted versus normalized position, which varies from -1 to 1 between the cylinders. While the normalized velocity profile only depends on G/D at low G/D (curves for different $Re_{U_G,G}$ collapse), at high G/D the shape of the profile becomes dependent on both $Re_{U_G,G}$ and G/D. In the limit of high Re (but still laminar flow), we would expect boundary layers to shrink and the interactions between cylinders to disappear. In this limit, normalized velocity in the gap center would approach unity and the velocity profile would resemble the superposition of the profiles for two non-interacting cylinders. That is, a peak would occur near each cylinder surface due to the velocity speedup that occurs even for flow around an isolated cylinder, forming double-peaked velocity profiles in the gaps of the array. At the highest G/D we studied, this is beginning to happen as the boundary layers around the neighboring cylinders become distinct instead of merged. Thus, for this parameter space, the velocity field between closely spaced cylinders exhibits fully overlapping boundary layers and velocity profiles proportional to U_0, while

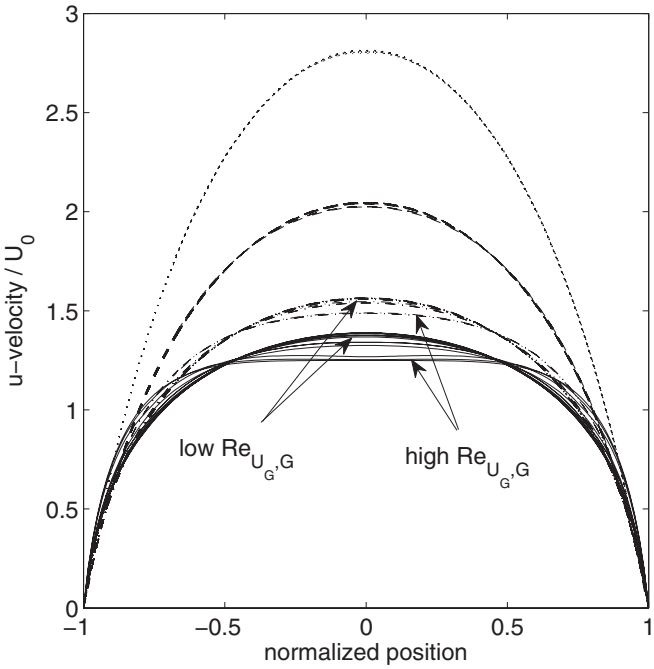

Figure 4. Profiles of normalized streamwise velocity component versus normalized position in the gap for all $Re_{U_G,G}$ and G/D studied. Most profiles collapse onto four groups of curves corresponding to G/D and are independent of $Re_{U_G,G}$, except where noted. $\cdots$, G/D 1; $---$, G/D 2; $-\cdot-$, G/D 5; —, G/D 10.

the flow fields for the highest G/D we studied entered a different flow regime with a region of nearly constant velocity and low shear in the middle of the gap, and an increasing dependence on $Re_{U_G,G}$.

2.2.2. Odorant concentration field. A representative series of odorant field snapshots is shown in figure 5, from when the odorant filament first reaches the array to when the bulk of the filament has advected far beyond the array. High shear in the velocity field in the gap causes the filament to 'bend' around each cylinder of the array, distorting it significantly and transforming the streamwise concentration gradient in the original filament to a cross-stream gradient within the gap. Concentration profiles in the gap over time are shown in figure 6. As the filament enters the gap, the profile is single-peaked, but because the odorant becomes trapped in the boundary layers around the cylinders, it develops a double-peaked shape as the bulk of the filament advects past the array. The peaks near the sensors then diminish due to both odorant flux and slow but persistent advection within the boundary layer.

Concentration profiles for several other $Re_{U_G,G}$, G/D and D/L are shown in figure 7, all at times near when peak flux occurred (the concentration field output was not saved exactly when peak flux occurred for all simulations). The profiles are double peaked for all cases except the lowest $Re_{U_G,G}$ tested ($Re_{U_G,G} = 0.06$), in which the gap velocity is slow enough that most of the odorant filament is still in the gap when peak flux occurs. Concentration boundary layer thickness, defined as the distance from the cylinder surface to where concentration

Table 1. Parameter ranges of this study and selected morphologies. A constant odorant filament width of $L = 0.56$ mm is assumed. Values for *G. falcatus* based on measurements by Mead and Koehl (2000); U_G calculated as leakiness $\cdot\, U_0$. Values for *P. argus* from measurements by Goldman and Koehl (2001) and Reidenbach *et al* (2008). Parameters that differ between real, finite extent appendages (i.e. measurements) and our infinite array models are labeled as such.

	U_0 (cm s^{-1}) finite	$Re_{U_0,D}$ finite	D (μm)	G (μm)	G/D	U_G (cm s^{-1})	$Re_{U_G,G}$	U_0 (cm s^{-1}) infinite	$Re_{U_0,D}$ infinite	$Pe_{U_G,G}$	D/L
Min tested	–	–	10	10	1	0.24	0.06	0.12	0.03	60	0.018
Max tested	–	–	50	500	10	40	22	20	2	22 000	0.089
G. falcatus juvenile return	1.2	0.12	10	103	10.3	0.3	0.32	0.27	0.027	319	0.018
G. falcatus juvenile flick	2.5	0.26	10	103	10.3	1.5	1.6	1.4	0.014	1593	0.018
G. falcatus adult return	3.9	0.80	20	96	4.8	0.98	0.96	0.81	0.16	965	0.036
G. falcatus adult flick	7.8	1.6	20	96	4.8	3.5	3.5	2.9	0.58	3474	0.036
P. argus adult return	2	0.5	20	100	5	0.01	0.01	0.0083	0.0017	10	0.036
P. argus adult flick	9	2	20	100	5	0.24	0.24	0.20	0.040	240	0.036

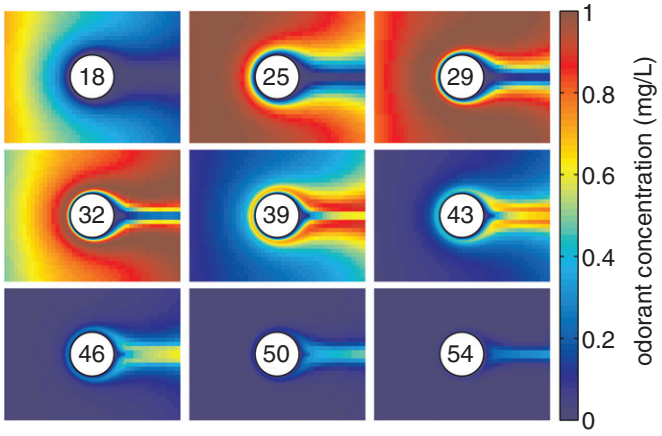

Figure 5. False-color renderings of odorant concentration in the vicinity of a cylinder in the array at consecutive times indicated by values inside circles (milliseconds) for $Re_{U_G,G} = 3$ ($U_0 = 2$ cm s^{-1}), $G/D = 2$, $D/L = 0.05$. Spatial scale is the same as figure 3, with $D = 50$ μm and $L = 0.56$ mm.

equals 99% of the instantaneous peak value in the gap, reaches 78% to the center of the gap in this case. This indicates that at very low $Re_{U_G,G}$, such as that of a *P. argus* return stroke (table 1), chemical interactions between odorant molecules and the aesthetasc cuticle are likely to extend significantly into the gaps between hairs.

The corresponding time series of the odorant flux into a cylinder of the array is shown in figure 8. For comparison, a hypothetical time series of the odorant concentration at the leading edge of the array is also shown, determined from equation (1) as if the array were not there. In figures 5, 6 and 8, time has been shifted so that $t = 0$ corresponds to when the leading edge of the undisturbed odor filament reaches the leading edge of the array. The shape of the time flux series is very nearly Gaussian like that of the odorant filament being sampled. However, the flux time series is slightly wider than the concentration time series and there is a slight amount of asymmetry around the centroid (not present in the undisturbed odorant filament or hypothetical concentration time series), with slightly more odorant mass under the right tail than

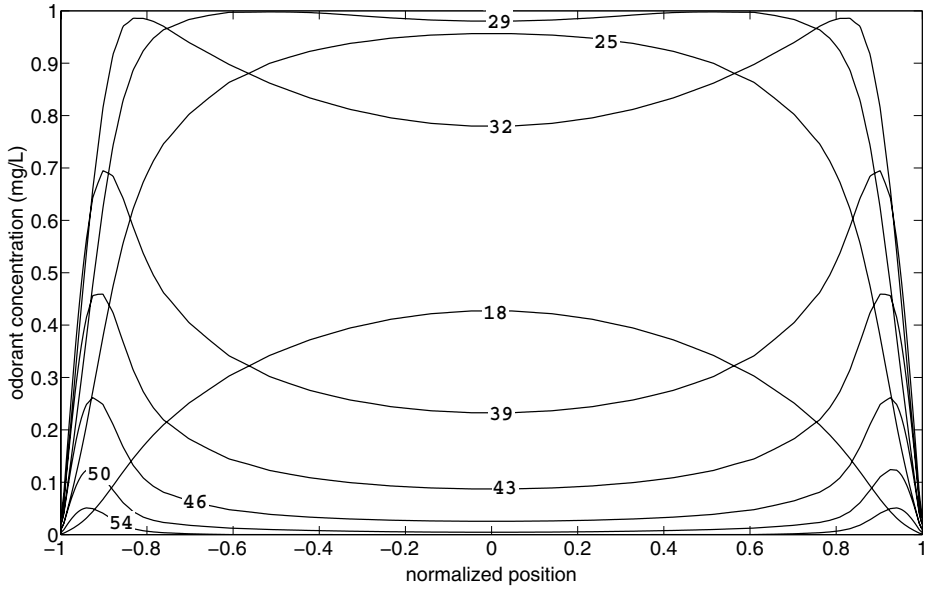

Figure 6. Odorant concentration profiles over time across the gap for $Re_{U_G,G} = 3$ ($U_0 = 2$ cm s^{-1}), $G/D = 2$, $D/L = 0.089$. Labeled times (milliseconds) correspond to those in figure 5.

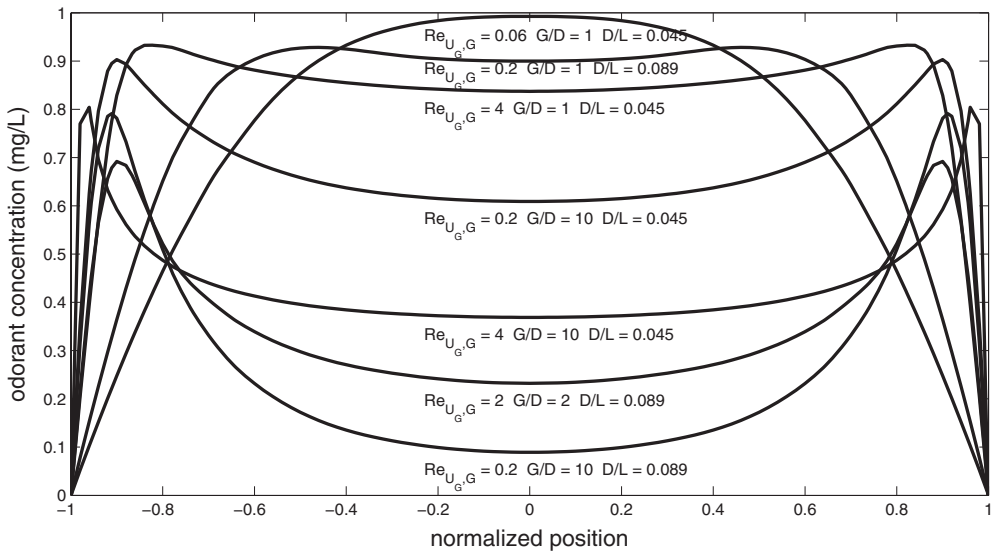

Figure 7. Odorant concentration profiles across the gap for various $Re_{U_G,G}$, G/D and D/L (labeled below each curve) at times near to when peak flux occurred, where 'near' is defined as within the smallest time interval that contains 33% of the total flux F_{total} for each simulation.

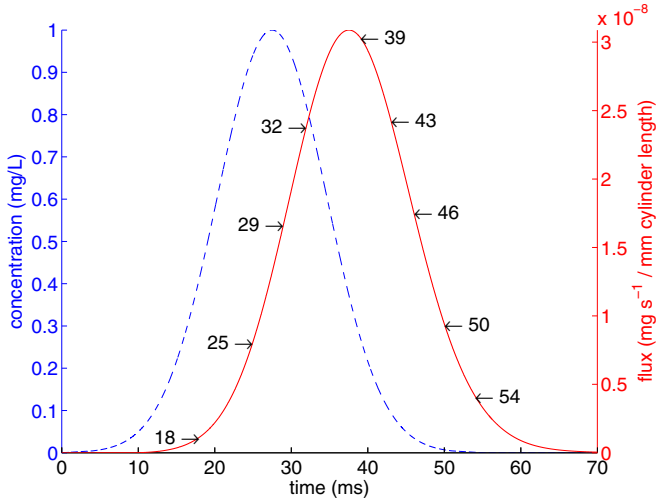

Figure 8. Time series of undisturbed odorant concentration at the cylinder's leading edge (dashed) and odorant flux into the cylinder (solid) for $Re_{U_G,G} = 3$ ($U_0 = 2$ cm s^{-1}), $G/D = 2$, $D/L = 0.089$ with marked times (milliseconds) corresponding to frames depicted in figure 5.

the left. Also note the ~10 ms lag between concentration and flux due to the slow velocity boundary layer around the cylinder; peak odorant flux (shortly before the fifth pane, 39 ms, in figure 5) occurs long after the concentration peak of the filament has passed by the cylinder.

2.2.3. Flux time series shape parameters. The signal filtering characteristics of the sensor array are represented by the differences in the shape of the unaltered incoming odorant filament and the flux time series output by the array. These shape differences are especially important if one's goal is to simply measure the microscale plume structure (e.g. with field instrumentation). We focus on three dimensionless shape parameters: normalized duration (or width) w^{norm}, skewness and excess kurtosis, to quantify these differences. The duration of the flux time series w is defined as the smallest time interval that contains 95% of the total odorant flux (equation (2)), and it is normalized to w^{norm} by using free-stream velocity U_0 and filament width $L = 0.56$ mm (equation (3)); this essentially compares the temporal duration of the flux time series to the equivalent temporal duration of the undisturbed odorant filament as it advects past in the reference frame of the array. Skewness and kurtosis of the flux time series are determined by calculating normalized central moments of the flux time series $f(t)$ according to equations (4) and (5):

$$w = \min(t_2 - t_1) \mid \int_{t_1}^{t_2} f(t)\,\mathrm{d}t = 0.95(F_{\text{total}}) \tag{2}$$

$$w^{\text{norm}} = w/(L/U_0) \tag{3}$$

$$\text{skewness} = \frac{\mu_3}{\sigma^3} \tag{4}$$

$$\text{kurtosis} = \frac{\mu_4}{\sigma^4} - 3 - \kappa_0, \tag{5}$$

where

$$\mu_k = \frac{\int_{-\infty}^{\infty} (t-\mu)^k f(t)\,\mathrm{d}t}{\int_{-\infty}^{\infty} f(t)\,\mathrm{d}t}$$

$$\mu = \frac{\int_{-\infty}^{\infty} t\, f(t)\,\mathrm{d}t}{\int_{-\infty}^{\infty} f(t)\,\mathrm{d}t}$$

$$\sigma = \sqrt{\mu_2}.$$

The skewness of the incoming Gaussian-linear odorant filament is zero, since it is symmetric, and its excess kurtosis κ_0 is about 0.01 (above the kurtosis of a pure Gaussian, equal to 3) due to the finite linear tails. We normalize the excess kurtosis (shortened to 'kurtosis' from here on) of the flux time series to that of the incoming filament by subtracting this preexisting (though very slight) kurtosis.

A simulation is ended when the flux of odorant into the cylinder (the time series in figure 8) has become sufficiently small. In practice, we found that the higher moments of the

flux time series, skewness and kurtosis were very sensitive to the tails of this curve, and convergence of these parameters to a maximum of 10% error was the determining factor in how long a simulation was run for.

2.3. Calculation of flux metrics

In addition to the three time series shape parameters outlined in section 2.2.3, we examine three metrics of flux, introduced in section 1.2, that are more directly related to biological odorant detection: peak flux, peak onset slope (or simply peak slope) and time-integrated or total flux.

The peak flux is simply taken as the maximum value of the flux time-series (near $t = 39$ ms for the simulation in figures 5, 6 and 8). The peak onset slope is estimated by calculating the time derivative of the flux time series using central differences, and taking the maximum of this approximate derivative. The peak onset slope occurs nearest to $t = 29$ ms for the simulation in figures 5, 6 and 8. The total flux is calculated by integrating the flux time series using the trapezoidal approximation. In the solver, a CFL condition due to the explicit hyperbolics limits the timestep to be very small relative to the timescale of flux variation, and flux data points are very closely spaced (e.g. 45 000 data points in figure 8). Hence, the errors due to the approximations used to calculate flux metrics are small compared to the error in the flux time series itself.

For the outer values of the parameter space we covered, convergence of the flux metrics (peak flux, peak onset slope, total flux) was investigated versus grid resolution at the finest level of local refinement near the cylinder and the number of cells in each dimension was doubled until a maximum of 10% difference between solutions was achieved. In addition to grid resolution, the effects of the inflow and outflow boundaries were tested. This is critical for low Re flows, when boundary effects can be extremely large (Loudon *et al* 1994, Lange *et al* 1998). The domain length (in the streamwise direction) was repeatedly doubled until a maximum of 10% difference between solutions was achieved. Once sufficient grid resolutions and domain sizes were determined for the corners of the parameter space, the most conservative values were chosen for all other combinations of parameters.

2.4. Dimensionless groups

Here we present a dimensional analysis of this problem. The variables of interest are the three flux metrics:

F_{peak} peak flux (mg m^{-1} s^{-1})

F_{slope} peak onset slope (mg m^{-1} s^{-2})

F_{total} time-integrated (total) flux (mg m^{-1}).

Each flux metric depends on the following seven independent variables:

U_0 inflow velocity (m s^{-1})

D cylinder diameter (m)

G gap between cylinders (m)

ν kinematic viscosity of water (m^2 s^{-1})

k_D molecular diffusivity of odorant in water (m^2 s^{-1})

C_0 peak concentration of the odorant filament (mg m^{-3})

L width of the odorant filament (m).

Here we neglect the effect of approximating the Gaussian tails as linear, and assume that the odorant filament's shape is determined solely by C_0 and L. Since neither C_0 or L were varied in this work, the odorant filament shape was constant in all simulations.

As each flux metric plus the seven variables that determine it sums to eight quantities consisting of three dimensional units (mass, length, time), five dimensionless groups are required to describe each flux metric. We choose the following normalizations to non-dimensionalize the flux metrics:

$$F^{\text{norm}}_{\text{peak}} = \frac{F_{\text{peak}}}{C_0 k_D} \quad \text{normalized peak flux}$$

$$F^{\text{norm}}_{\text{slope}} = \frac{F_{\text{slope}} L^2}{C_0 k_D^2} \quad \text{normalized peak slope}$$

$$F^{\text{norm}}_{\text{total}} = \frac{F_{\text{total}}}{C_0 L^2} \quad \text{normalized time-integrated (total) flux,}$$

and the following four dimensionless groups they depend on:

$$Pe_{U_G,G} = \frac{U_G G}{k_D} \quad \text{gap-based Peclet number}$$

G/D gap to diameter ratio

D/L sampling fraction

ν/k_D Schmidt number.

The normalizations of the flux metrics are not intuitive, but were chosen for convenience: because we did not vary C_0, k_D or L, the effect of our normalizations is simply to scale the dimensional flux metrics by the same amount across all simulations. If we had chosen a more intuitive set of normalizations that utilized parameters we did vary (e.g. D, G, U_0), our results would be framed in a different context as they would represent a comparison to another dynamically changing system (e.g. a type of virtual sensor) rather than mimicking the behavior of the dimensional flux metrics. Although comparisons to a virtual sensor can be useful since they normalize to theoretical limits, here we examine the absolute performance of sensor arrays. However, our normalizations come with the caveat that C_0, k_D, and L *must be viewed as constants* when interpreting trends in $F^{\text{norm}}_{\text{peak}}$, $F^{\text{norm}}_{\text{slope}}$ and $F^{\text{norm}}_{\text{total}}$.

We use a gap-based Peclet number $Pe_{U_G,G}$ to describe how much advection dominates diffusion as odorant is transported within the array. We believe scaling with U_G is more appropriate than U_0 since U_G more directly describes the fluid dynamics near the sensors where flux takes place. For the infinite arrays studied here, this seems especially appropriate because of the sometimes large increase in flow speed as fluid is forced through the array gaps. The choice of G for a length scale is more arbitrary; D may be equally appropriate. In addition to the relative importance of advection versus diffusion, $Pe_{U_G,G}$ can also describe the interactions between cylinders. When $Pe_{U_G,G}$ is maximized via U_G and G, there is fast flow between distant cylinders, and when $Pe_{U_G,G}$ is minimized, there is slow flow between close cylinders. Hence,

one would expect boundary layer interactions (concentration and momentum) between cylinders to be strong at low $Pe_{U_G,G}$ and weak at high $Pe_{U_G,G}$, given constant ν and k_D.

G/D is an aspect ratio describing how sparse the array of sensors is, and like $Pe_{U_G,G}$, describes the interactions between cylinders in the array. Dense arrays are expected to have overlapping boundary layers between cylinders, and as G/D increases, the interactions between cylinders diminish (see figure 4). It is important to keep in mind that for infinite arrays, denser arrays sampling at the same speed experience higher fluid velocities in the gaps due to mass conservation, whereas denser finite arrays often experience lower gap velocities due to low leakiness.

D/L describes the size of the sensors compared to the thickness of the odorant filament. One interpretation of D/L is the ratio of array volume to filament volume, or 'sampling fraction'. A high sampling fraction indicates that much or all of the odorant filament can fit within the gaps of the array, while a low sampling fraction indicates that only a small region of the filament is sampled at a given moment.

A similar dimensional analysis can be done for aspects of the fluid flow only, such as velocity profiles and shear rates. This would yield a Reynolds number $Re_{U_G,G}$ instead of $Pe_{U_G,G}$, and G/D as the two governing groups.

Note that because we did not vary the Schmidt number ($Sc = 10^3$ for small molecules in seawater), $Pe_{U_G,G}$ and $Re_{U_G,G}$ always differ by a constant factor of 1000 and Sc is omitted from the analysis from here on. More data would be needed to understand how the functional relationships presented in this work would change if the sensor arrays were operated in a different fluid such as air.

2.5. Parameter space

The objective of this work is to understand the effects of array geometry and sampling speed on the flux time series generated by the array. To this end, we varied the sampling speed U_0, the gap between sensors G and the diameter of each sensor D. Parameter ranges we studied are summarized in table 1 as 'min tested' and 'max tested', along with values known for two crustacean species, the mantis shrimp *G. falcatus* (juvenile and adult) and spiny lobster *P. argus* (adult).

For an infinite array of cylinders, the average fluid speed in a gap can easily be determined in terms of the sampling speed from mass conservation:

$$U_G = U_0 \left(1 + \tfrac{1}{G/D}\right).$$

The average gap velocity U_G of an infinite array is always higher than the gap velocity of a corresponding (same inflow velocity U_0 and G/D) finite length array. This causes the leakiness (see section 1.2) of an infinite array, defined as $U_G/U_0 = 1 + \frac{1}{G/D}$, to be always greater than unity. Koehl and coworkers noted a parameter range ($Re_{U_0,D} = 10^{-2}$–10^1 and G/D = 1–15) in which leakiness of finite length arrays varied strongly from about 0.06–0.95 (Koehl 1992, 1996). It is likely that scalar transport also varies strongly in this flow regime. Although infinite arrays cannot reproduce the low leakiness that finite arrays can exhibit, both geometries may experience similar local flow in the immediate vicinities of the cylinders, where flux occurs. To better match this local flow, one can use $Re_{U_G,G}$, based on flow between cylinders, instead of the traditional $Re_{U_0,D}$. Koehl *et al* 's results can be converted by multiplying their reported leakiness, $Re_{U_0,D}$, and G/D values to obtain $Re_{U_G,G}$. The critical parameter range of finite arrays is then predicted to be $Re_{U_G,G} = 10^{-3}$–10^1. Here, we varied G/D and U_0 to achieve $Re_{U_G,G}$ of 0.06–22 (table 1), which falls within the predicted critical range of biological importance.

2.6. Curve fits

The shape parameters w^{norm}, skewness, and kurtosis and flux metrics $F^{\text{norm}}_{\text{peak}}$, $F^{\text{norm}}_{\text{slope}}$ and $F^{\text{norm}}_{\text{total}}$ were fit to the following five-parameter power law function of $Pe_{U_G,G}$, G/D and D/L (Sc is not included since it was not varied):

$$\text{fitted value} = M\left(Pe_{U_G,G}\right)^a (G/D)^b (D/L)^c + I. \quad (6)$$

The fits were performed in MATLAB (2010a, The Mathworks, Natick, MA) using the nonlinear least-squares optimization function lsqnonlin() in the Optimization Toolbox. Since the magnitude of the flux metrics was typically about 10^{-8}, to avoid numerical precision problems, the data were rescaled temporarily when necessary to perform the curve fitting. Since negative values for $F^{\text{norm}}_{\text{peak}}$, $F^{\text{norm}}_{\text{slope}}$ and $F^{\text{norm}}_{\text{total}}$ would be physically impossible, we constrained I for these fits to be non-negative, but did not constrain I for w^{norm}, skewness or kurtosis.

2.7. Predictions for real olfactory appendages

Our model allows us to predict aspects of the signal distortion (i.e. w^{norm}, skewness and kurtosis) introduced by real olfactory antennules. To mitigate the differences between our infinite array model and real finite arrays, we limited ourselves to species for which the gap velocity between aesthetascs is known or can be estimated from published data so that we could calculate the appropriate $Pe_{U_G,G}$. Gap velocities for the adult spiny lobster *P. argus* were obtained from measurements of velocity fields around the aesthetascs of physical models (Reidenbach *et al* 2008), and for the juvenile and adult mantis shrimp *G. falcatus* by multiplying published leakiness and freestream velocity values, also obtained using physical models (Mead and Koehl 2000). We used these gap velocities together with published measurements of aesthetasc diameter and gap width (Mead *et al* 1999, Goldman and Koehl 2001) to estimate $Pe_{U_G,G}$, G/D and D/L for these real olfactory hair arrays sampling a 0.56 mm odor filament. We then predicted the duration w of the flux into aesthetascs during the rapid downstroke or outstroke using the power law equation for w^{norm} described in section 2.6 and the definition of w^{norm} given in section 2.2.3. Skewness and kurtosis for *P. argus* and *G. falcatus* inspired infinite arrays were also predicted using our curve fits.

3. Results and discussion

3.1. Flux time series distortion

The ranges of the flux time series shape parameters over our parameter space give an overview of the signal filtering properties of the sensor arrays. Normalized durations (w^{norm})

Table 2. Power law regressions of flux time series shape parameters and flux metrics. Fitted value $= M\left(Pe_{U_G,G}\right)^a (G/D)^b (D/L)^c + I$. Ranges of predicted values across the parameter space are also given. k_D, C_0 and L should be treated as constant due to our normalization method for the flux metrics.

Fitted value	a	b	c	M	I	R^2	min	max
w^{norm}	0.30	0.48	1.7	0.54	0.99	0.993	1.0	1.5
Skewness	0.52	0.39	1.8	0.20	−0.011	0.982	2.9E-4	1.0
Kurtosis	0.93	0.27	2.2	0.033	−0.091	0.984	−0.08	2.9
$F^{\text{norm}}_{\text{peak}}$	0.32	−0.5	−0.068	2.89	2.2E-14	0.992	9.6	52
$F^{\text{norm}}_{\text{slope}}$	1.3	−1.2	−1.1	3.3	2.3E-10	0.997	2.1E4	1.4E7
$F^{\text{norm}}_{\text{total}}$	−0.68	0.26	0.99	4.4	2.4E-5	0.996	1.8E-4	0.013

of the flux time series range from 1.0 to 1.5 over the parameter space we investigated (table 2). Since the lower limit of w^{norm} is not very different from unity, the effect of the array over this parameter range is to either broaden the sampled filament or leave its temporal width essentially unchanged. All skewness values of the flux time series are positive (range 2.9E-4–1.0, table 2), indicating that the tail of the flux time series is always 'heavier' than the lead-in to some degree. Kurtosis varies from nearly zero (minimum −0.08, table 2) to higher than the nearly Gaussian odorant filament (maximum 2.9) at high $Pe_{U_G,G}$, G/D and D/L. Thus, although these arrays only seem capable of increasing the perceived width of the sampled filament, they can simultaneously make it appear more 'peaked.'

The power laws summarized in table 2 appear to fit the data well, with the lowest R^2 value being 0.982. The curve fits indicate that w^{norm}, skewness and kurtosis all display direct relationships with $Pe_{U_G,G}$, G/D and D/L. All three shape parameters are most sensitive to the sampling fraction D/L with approximately quadratic dependence, indicating that for flux time series shape, the interplay between array geometry and filament structure is more important than parameters only describing the sensor array ($Pe_{U_G,G}$ and G/D). This is consistent with the ability of these arrays to sample fine scale plume structure, since a strong relationship between plume structure and the flux time series would be necessary to do so, as opposed to the flux time series being mostly determined by the properties of the array alone.

As an odorant filament is advected through the array, a portion of odorant mass appears to become trapped in the low-velocity boundary layer around each cylinder of the array (figure 3) for a relatively long period of time (figure 5). The hold-up of odorant could cause the delay in peak flux, broad width and positive skewness that we often see in the flux signal. Our flux time series, which would always be essentially Gaussian if not for the physical presence of the array, bear some resemblance to concentration time series measured at a point in many tracer release experiments, in both laminar and turbulent shear flows, that are designed to test theories of shear (Taylor) dispersion (Young and Jones 1991). In these studies, the unexpected skewness is often attributed to scalar trapping in the viscous sublayer near boundaries or dead zones in the flow such that insufficient time has occurred for complete transverse mixing, violating a necessary condition for Taylor's approximation. We can make a similar argument here: if the time required for odorant molecules to traverse the gap via diffusion was very small compared to their residence time within the gap, then we would expect a Gaussian-shaped flux time series, as the array would act as a rapid and complete sink for the incoming Gaussian concentration profile. However, if we take the ratio of odorant residence time D/U_G to the diffusion timescale $\left(\frac{1}{2}G\right)^2/k_D$ (this ratio is equivalent to $4\left(Pe_{U_G,G}\right)^{-1}(G/D)^{-1}$), we find that this quantity is indeed much less than unity for our entire parameter space (max 0.07). This indicates that transverse mixing via diffusion in the gap is by no means complete. Instead, a large fraction of odorant mass appears to pass through the gap unsensed, while the remainder is trapped in the boundary layer around and directly behind each cylinder and diffuses inside.

3.2. Flux metrics

Table 2 summarizes the power law fits of $F^{\text{norm}}_{\text{peak}}$, $F^{\text{norm}}_{\text{slope}}$ and $F^{\text{norm}}_{\text{total}}$ to $Pe_{U_G,G}$ and G/D and D/L, with excellent fits indicated by the high R^2 values. Interestingly, our dependence of $F^{\text{norm}}_{\text{peak}}$ on the Peclet number ($\propto Pe^{1/3}_{U_G,G}$) is the same as the dependence of the steady state scalar flux on Pe for an isolated sphere at $Re = 0.1$, given by Friedlander (1957). This suggests that a pseudo-steady state approximation might be valid for the case of unsteady sampling of an odorant filament, since a 0.56 mm filament is much larger than 10–50 μm aesthetascs.

The exponents in table 2 indicate that $F^{\text{norm}}_{\text{peak}}$ and $F^{\text{norm}}_{\text{slope}}$ both increase with $Pe_{U_G,G}$ and decrease with G/D and D/L, with the strength of the dependences being higher for $F^{\text{norm}}_{\text{slope}}$ than for $F^{\text{norm}}_{\text{peak}}$. The peak slope is intuitively expected to be more sensitive than the peak flux because it is a property of the derivative of the flux time series versus the time series itself. $F^{\text{norm}}_{\text{total}}$ displays the opposite trends, decreasing with $Pe_{U_G,G}$ and increasing with G/D and D/L. The physical interpretations of the non-dimensional groups can help explain these trends, although we caution that due to our normalization method (section 2.4), k_D, C_0 and L should be treated as constants. In particular, D/L should be interpreted as the effect of varying D only so that trends in $F^{\text{norm}}_{\text{peak}}$, $F^{\text{norm}}_{\text{slope}}$ and $F^{\text{norm}}_{\text{total}}$ accurately represent trends in the absolute performance metrics F_{peak}, F_{slope} and F_{total}.

The gap Peclet number $Pe_{U_G,G}$ combines aspects of array geometry (G) and sampling kinematics (U_G) with scalar diffusivity (k_D) to represent the relative importance of advective to diffusive transport of odorant within the array. Since $F^{\text{norm}}_{\text{peak}}$ and $F^{\text{norm}}_{\text{slope}}$ occur at instants in time, to obtain high values it is most important to bring the peak of the filament close to the sensor surface, via advection, so that the final diffusive step may occur rapidly. Diffusive

transport decreases the peak slope and peak flux by smoothing peaks in the concentration field before they reach the sensor. This is in agreement with the experimental work by Moore *et al* (1991) on the odorant sampling properties of the various chemosensory appendages of the clawed lobster *H. americanus*; slower flow in the immediate vicinity of the sensory hairs caused lower peak concentrations and larger widths of the odorant pulse they were exposed to compared to the original free-stream pulse. Oppositely, $F^{\text{norm}}_{\text{total}}$ is increased by a lower $Pe_{U_G,G}$ transport regime in which diffusion becomes more important. This is because signal smoothing is inconsequential to total flux, and the effects of diffusion integrated over the sampling event bring more odorant molecules to the sensor surface than would occur at high $Pe_{U_G,G}$.

G/D represents the sparsity of an array of sensors. As seen in figure 4, denser infinite arrays with low G/D have generally steeper, more parabolic velocity profiles than sparse arrays, and achieve higher velocity speed-ups in the gap relative to the freestream velocity. Arrays at low G/D experience a relatively high shear rate over most of the gap, causing the odorant filament to undergo more stretching around the sensors compared to arrays at high G/D. This moves more of the central odorant peak close to the sensor surfaces, resulting in the higher $F^{\text{norm}}_{\text{peak}}$ and $F^{\text{norm}}_{\text{slope}}$ that we see at low G/D. However, the higher shear at low G/D also results in lower $F^{\text{norm}}_{\text{total}}$, a tradeoff for which we do not have a detailed explanation.

D/L, the sampling fraction, represents the ratio of sensor size, or streamwise array width, to filament width. The sampling fraction describes how much of the filament is sampled at any instant in time and the extent to which spatial integration over a sensor results in loss of information contained in the plume structure. However, increasing D/L via D also acts to increase the surface area available for flux, allowing more odorant molecules to be captured. D/L can thus describe a tradeoff between the array surface area and signal smoothing. Consequently, $F^{\text{norm}}_{\text{peak}}$ displays only a slightly negative correlation with D/L, the effects of spatial integration largely offset by increased surface area. On the other hand, $F^{\text{norm}}_{\text{slope}}$ is somewhat decoupled from the magnitude of the odorant flux since $F^{\text{norm}}_{\text{slope}}$ is a property of the time series' temporal derivative. Hence, the surface area does not directly affect the peak slope and it is inversely related to the sampling fraction due to the signal smoothing effect. In contrast to the peak metrics, $F^{\text{norm}}_{\text{total}}$ increases with D/L (i.e. as D increases) because more odorant molecules in the filament can be captured at any moment (the filament becomes narrow relative to the array) and signal smoothing does not adversely impact $F^{\text{norm}}_{\text{total}}$ since it is a time-integrated quantity.

3.3. Application to real olfactory arrays

3.3.1. Signal distortion. Table 3 summarizes the predicted flux time series shape parameters for the antennules of the spiny lobster *P. argus* and the juvenile and adult stages of the stomatopod *G. falcatus*. The normalized duration of flux w^{norm} is nearly unity for all cases, indicating that these chemosensory hair arrays do not distort the observed temporal width of the filament. Similarly, the flux time series generated by these arrays are predicted to introduce almost no skewness or kurtosis compared to the original odorant filament shape. Even though the antennules of spiny lobsters and mantis shrimp distort the spatial structure of an odorant filament at the scale of the aesthetascs by physically intercepting it, the predicted flux time series is still an excellent representation of the filament's original structure. Thus, if low signal distortion is desired, the antennules of *P. argus* or *G. falcatus* seem to be reasonable starting points for the design of an artificial sensor array tasked with sampling small-scale turbulent plume structure in water.

Table 3. Predicted durations and shape parameters of flux time series for *P. argus* and *G. falcatus* during the rapid downstroke or outstroke, respectively, for both this study and the work of Stacey *et al* (2002). Italicized values are extrapolated.

	w (ms)	w^{norm}	Skewness	Kurtosis
		Stacey *et al*		
Juvenile *G. falcatus*	40	1.00	NA	NA
Adult *G. falcatus*	12	0.94	NA	NA
		This study		
Juvenile *G. falcatus*	41	1.0	0.0054	−0.083
Adult *G. falcatus*	20	1.0	0.053	−0.026
Adult *P. argus*	6.3	*1.0*	*0.0091*	*−0.0864*

The strongest predictor of signal distortion is D/L (section 3.1). Therefore, using very small sensors is expected, not surprisingly, to greatly enhance the ability of an artificial nose to measure fine-scale plume structure. Individual sensors as small as the Batchelor scale (the spatial scale of the smallest chemical fluctuations, $O(10\ \mu\text{m})$ in typical benthic boundary layer flows) are within reach given current technological trends (James *et al* 2005).

3.3.2. Flux metrics. To summarize the trends in section 3.2, a high $Pe_{U_G,G}$, low G/D, low D/L array will generate a sharp (high onset slope) time series with a high peak flux, but will detect fewer odorant molecules in total. This trade-off may have important neurobiological consequences, since olfactory neurons respond more strongly (i.e. exhibit higher spiking frequency) to more concentrated odorant pulses (Gomez and Atema 1996b) but likely also require a certain threshold F_{total} to respond at all though the threshold might be quite low. Similarly, Liao and Cowen (2002) suggest that the sensors of an engineered plume-tracing agent should be capable of sampling both sharp gradients and very low concentrations; our results suggest that these properties may be mutually exclusive.

Recently, Page *et al* (2011a) found that the upstream movement by plume-tracking crabs is well predicted, in a binary fashion, by antennular encounters with peak odorant filament concentrations above a certain threshold. In our model of crustacean aesthetasc arrays, the peak flux of odorant into aesthetascs is proportional to the peak concentration; hence, a high peak flux might be required for upstream

movement. Although the odorant flux is affected by both plume structure and how the plume is sampled, $F_{\text{peak}}^{\text{norm}}$ varies over less than an order of magnitude over our entire parameter space (table 2) of array geometries and sampling speeds. The greater dependence of the peak flux on C_0 (linear) than on array properties is echoed by the power law exponents for $F_{\text{peak}}^{\text{norm}}$ in table 2, whose absolute values are all substantially less than unity. Furthermore, the minimum concentration in a turbulent plume is essentially zero, resulting in a huge dynamic range of sampled concentrations as an animal flicks its antennules. The peak flux may therefore be mostly determined by the plume structure, and if it is only important in a binary fashion, an organism's (or robot's) plume tracking performance might not be sensitive to its precise morphology and sampling kinematics.

3.3.3. Flux time series duration. The duration of the flux time series is an important quantity because it determines approximately how long olfactory neurons or chemical sensors are exposed to odorant during a sampling event. Here we focus on the biological implications with some concluding remarks on artificial systems.

Olfactory neurons require a certain period of stimulation to detect and quantify an odorant. For example, antennule olfactory neurons of *Homarus americanus*, the clawed lobster, need 50 ms of exposure to an odorant to detect it and 200 ms to measure its concentration (Gomez and Atema 1996b). On the other hand, adaptation (decreased response to the odorant) acts to diminish the effect of odorant flux at long exposure time; *H. americanus* olfactory neurons begin adapting to a stimulus in as little as 300 ms (Gomez and Atema 1996b). The relatively narrow range between the stimulus integration time of 200 ms and the beginning of adaptation at 300 ms means that lobster olfactory neurons may be tuned to a fairly precise duration of stimulation. Indeed, this time window matches the flicking frequency of *H. americanus* antennules, 4–5 Hz (Gomez and Atema 1996a).

Koehl *et al* showed that for a real *P. argus* antennule sampling a real turbulent dye plume, the spatial pattern of the chemical filaments in the aesthetasc array at the end of a flick is retained during the return stroke and inter-flick pause (Koehl 2001a). It has been hypothesized that in antennule-flicking crustaceans like lobsters, the slow return stroke and inter-flick pause enhance the odorant flux by trapping the odorant within the array and allowing more time for diffusion, and presumably stimulation of neurons, to occur (Mead *et al* 1999, Mead and Koehl 2000, Goldman and Koehl 2001, Reidenbach *et al* 2008). To investigate this idea, we predicted (see section 2.7 for details) the durations of odorant flux, and thus neural stimulation, during the outstroke and downstroke of *G. falcatus* and *P. argus*, respectively (table 3). Note that predictions for *P. argus* are extrapolated outside the convex hull of our parameter space (*P. argus* was originally an end member of a parameter space based on $Re_{U_0,D}$). Also included in table 3 are w and w^{norm} predicted by Stacey *et al* (2002), using velocity profiles measured around aesthetascs of dynamically scaled physical models of antennules of *G. falcatus*. Values in table 3 were visually estimated from plots of their flux time series. The differences between the predictions of Stacey *et al* and this study may be due to substantially different modeling approaches as well as our infinite array approximation. Although we define our *G. falcatus* and *P. argus* cases using $Re_{U_G,G}$ based on measurements in an attempt to account for differences in how infinite versus finite arrays operate (see section 2.5), we are currently exploring these differences further with simulations of sensor arrays of finite extent.

Our results indicate that for a 0.56 mm odorant filament, it only takes about 6 ms for *P. argus* chemosensors sampling at the downstroke velocity to achieve maximum total flux (table 3). For mantis shrimp, we predict maximum total flux in 41 and 20 ms for juvenile and adult stages, respectively, while Stacey *et al* predict 40 and 12 ms. These flux durations are worth comparing to both the duration of the actual downstroke and outstroke movement, since this study and Stacey *et al* effectively assume an infinitely long sweep through the water but real flicks do not continue forever, and the stimulus integration times of olfactory neurons, as discussed above.

In reality, *P. argus* takes approximately 150–200 ms to complete the flick downstroke (Goldman and Koehl 2001), and *G. falcatus* (juvenile and adult) takes about 33 ms for the outstroke (Mead *et al* 1999). Therefore, *P. argus* can certainly completely sample a 0.56 mm odorant filament during the downstroke, but in the case of *G. falcatus* the length of the downstroke may be limiting, especially for juveniles. Failure to intercept an entire odor filament would decrease the total flux but not necessarily affect the ability to capture the peak slope or peak flux.

Unfortunately there are no data on the stimulus integration times of *P. argus* or *G. falcatus* olfactory neurons, so we refer to the values for *H. americanus* here (i.e. 50 ms of stimulation needed for detection and 200 ms for quantification). These neural processing timescales are generally longer than the predicted flux durations for *G. falcatus* and especially *P. argus*. Therefore, the return stroke and inter-flick pause are indeed likely to be important to these animals by allowing ample time for neural stimulation to occur, as long as some odorant remains trapped in the array during these phases. The rapid advection of odor filaments through the aesthetasc arrays of *P. argus* and *G. falcatus* means that the width of a 0.56 mm odorant filament is unlikely to be measured via the duration of the flux.

Over our entire parameter space, we observed flux durations (w) from 3 to 470 ms. Although the upper end is within the detection limits of crustacean olfactory neurons, we cannot predict leakiness with our infinite array model, and this is likely to be a critical factor in the performance of real sensor arrays as it determines how much of an odorant patch can enter a finite array. Since our arrays could only stretch the temporal width of the original odorant filament by a maximum factor of 1.5 (max w^{norm}, table 2), the longer flux durations we observed were mainly due to slower sampling speeds than are the case for *P. argus* or *G. falcatus* flicks (e.g. 470 ms corresponds to the *P. argus* return stroke). We suspect that in reality, the cost of dramatically decreased odorant access at these sampling speeds would outweigh any advantage of increased flux duration.

It is useful to examine these flux durations in the context of diffusion of odorant through the aesthetasc cuticle. Although we assume a constant surface concentration of zero on each aesthetasc, it is likely that diffusion and/or consumption of odorant inside the aesthetasc will continue for some finite time. The diffusion depth for the odorant into an aesthetasc is of the order of $\sqrt{2k_D t}$, assuming a diffusivity equal to that of odorant in water; diffusion through the aesthetasc cuticle is likely to be slower than this estimate, and dependent on the molecular weight of the odorant (Derby *et al* 1997). A flux duration of 3 ms (lowest across our parameter space) thus corresponds to a diffusion depth of about 2.4 μm while a flux duration of 470 ms (highest across our parameter space) corresponds to a diffusion depth of about 31 μm. Hence, since the cuticle is typically 0.5–1 μm thick (Grunert and Ache 1988, Mead and Weatherby 2002), odorant/dentritic receptor interactions do not seem to be confined to either being purely a surface phenomenon or volumetric phenomenon over a biologically relevant parameter space.

We focus on the information a plume tracking agent receives via the flux time series generated by the sensor array as a whole. However, the odorant filament structure could also be inferred via spatial differences in flux throughout the array. For example, a filament's width could be estimated this way if it were oriented perpendicularly to the row of sensors. It is not known whether lobsters or mantis shrimp can use the spatial concentration distribution along an antennule to measure the filament width; this depends in part on how signals from individual aesthetascs are aggregated via neural convergence. Nonetheless, in principle, a bio-inspired olfactory antennule could measure the filament structure using both spatial and temporal information from its array of sensors.

The response times of most engineered chemical sensors currently in use are also too slow to resolve brief odorant bursts in either air or water (Ishida and Moriizumi 2004, Nakamoto and Ishida 2008, Vlasov *et al* 2010). Hence, we face a similar problem as crustaceans in translating temporal flux signals to high resolution odorant concentration maps, and analysis of spatial response data seems the more promising route if such maps are desired. The external location and morphology of olfactory antennules seems to facilitate spatial sampling, but artifical noses generally have a long way to go for this to be possible. The sampling systems of most electronic noses are quite ungainly, often employing separate 'preconcentrators' that collect odorant mass from a bulk fluid sample and then relay it to the actual sensors (e.g. via adsorption and subsequent desorption) (Settles 2005). Not only are such sampling methods slow, but they also obliterate any fine-scale plume structure. Crustacean aesthetasc arrays might be an elegant solution, as the sampling kinematics and dense hair spacing may facilitate odorant detection by slowly-responding sensors (via odorant trapping during the return stroke and pause), while the array-like morphology simultaneously may allow for direct spatial sampling.

4. Summary

To sample the fine-scale turbulent plume structure using physical contact sensors, an array of closely spaced, small sensors is needed. However, as a small-scale sensor array samples a plume, the physical presence of the sensors necessarily results in distortion of the original plume structure. We found that signal distortion increases with each of the three dimensionless groups that characterize this problem ($Pe_{U_G,G}$, G/D and D/L).

Flux-detecting olfactory sensors transduce spatial properties of odorant filaments into temporal properties of flux time series. We found that peak properties (peak flux, peak onset slope) of the flux time series are maximized by advection-dominated transport (high $Pe_{U_G,G}$) between densely spaced (low G/D), thin (low D/L) sensors, while the total flux is minimized by this sampling regime.

Since signal distortion is most sensitive to the sampling fraction D/L, flux-detecting chemical sensor arrays for use underwater should incorporate the smallest sensors possible if distortion is to be minimized. However, our analysis of trends in peak flux metrics and total flux indicates that preservation of odorant filament 'sharpness' and the ability to measure very low concentrations may be mutually exclusive design goals.

For chemical sensor arrays inspired by the specific morphologies and sampling kinematics of the spiny lobster *P. argus* and the mantis shrimp *G. falcatus*, the shape of a sampled odorant filament appears to be preserved quite well in the flux time series. However, our results also imply that the olfactory neurons of these species probably cannot detect the brief flux event resulting from interception of a single 0.56 mm odorant filament arriving parallel to the antennule. Current chemical sensing technology is similarly constrained. This suggests either that spatial differences in flux across the aesthetasc array are utilized by animals, or that malacostracan crustaceans (and bio-inspired robots) simply might not require such highly detailed information to track turbulent odorant plumes.

Acknowledgments

This research was supported by NSF grant IOS-0842681 to MK and used resources of the National Energy Research Scientific Computing Center, which is supported by the Office of Science of the US Department of Energy under contract no DE-AC02-05CH11231. We thank two anonymous reviewers for their comments on earlier versions of the manuscript.

References

Amrani M E H, Dowdeswell R M, Payne P A and Persaud K C 1997 An intelligent gas sensing system *Sensors Actuators* B **44** 512–6

Atema J 1985 Chemoreception in the sea: adaptations of chemoreceptors and behaviour to aquatic stimulus conditions *Symp. of the Society for Experimental Biology* pp 387–423

Atema J 1995 Chemical signals in the marine environment: dispersal, detection, and temporal signal analysis *Proc. Natl. Acad. Sci. USA* **92** 62–6

Barad M F, Colella P and Schladow S G 2009 An adaptive cut-cell method for environmental fluid mechanics *Int. J. Numer. Methods Fluids* **60** 473–514

Barlow H B 1958 Temporal and spatial summation in human vision at different background intensities *J. Physiol.* **141** 337–50

Cantor R S, Ishida H and Janata J 2008 Sensing array for coherence analysis of modulated aquatic chemical plumes *Anal. Chem.* **80** 1012–8

Carr W E S, Trapidorosenthal H G and Gleeson R A 1990 The role of degradative enzymes in chemosensory processes *Chem. Senses* **15** 181–90

Chan K Y, Fujioka H, Bartlett R H, Hirschl R B and Grotberg J B 2006 Pulsatile flow and mass transport over an array of cylinders: gas transfer in a cardiac-driven artificial lung *J. Biomech. Eng.—Trans. ASME* **128** 85–96

Chatterjee D, Biswas G and Amiroudine S 2009 Numerical investigation of forced convection heat transfer in unsteady flow past a row of square cylinders *Int. J. Heat Fluid Flow* **30** 1114–28

Cheer A Y L and Koehl M A R 1987a Fluid-flow through filtering appendages of insects *IMA J. Math. Appl. Med. Biol.* **4** 185–99

Cheer A Y L and Koehl M A R 1987b Paddles and rakes—fluid-flow through bristled appendages of small organisms *J. Theor. Biol.* **129** 17–39

Crimaldi J P, Koehl M A R and Koseff J R 2002 Effects of the resolution and kinematics of olfactory appendages on the interception of chemical signals in a turbulent odor plume *Environ. Fluid Mech.* **2** 35–64

Crimaldi J P and Koseff J R 2001 High-resolution measurements of the spatial and temporal scalar structure of a turbulent plume *Exp. Fluids* **31** 90–102

Crimaldi J P and Koseff J R 2006 Structure of turbulent plumes from a momentumless source in a smooth bed *Environ. Fluid Mech.* **6** 573–92

Crimaldi J P, Wiley M B and Koseff J R 2002 The relationship between mean and instantaneous structure in turbulent passive scalar plumes *J. Turbul.* **3** 1–23

DasGupta S and Waddell S 2008 Learned odor discrimination in drosophila without combinatorial odor maps in the antennal lobe *Curr. Biol.* **18** 1668–74

del Valle M 2010 Electronic tongues employing electrochemical sensors *Electroanalysis* **22** 1539–55

Derby C D, Cate H S and Gentilcore L R 1997 Perireception in olfaction: molecular mass sieving by aesthetasc sensillar cuticle determines odorant access to receptor sites in the Caribbean spiny lobster *Panulirus argus J. Exp. Biol.* **200** 2073–81

Fischer H B, List J E, Koh R C, Imberger J and Brooks N H 1979 *Mixing in Inland and Coastal Waters* (New York: Academic)

Friedlander S K 1957 Mass and heat transfer to single spheres and cylinders at low Reynolds numbers *AIChE J.* **3** 43–8

Gleeson R A 1982 Morphological and behavioral identification of the sensory structures mediating pheromone reception in the blue-crab *Callinectes sapidus Biol. Bull.* **163** 162–71

Goldman J A and Koehl M A R 2001 Fluid dynamic design of lobster olfactory organs: high speed kinematic analysis of antennule flicking by *Panulirus argus Chem. Senses* **26** 385–98

Goldman J A and Patek S N 2002 Two sniffing strategies in palinurid lobsters *J. Exp. Biol.* **205** 3891–902

Gomez G and Atema J 1994 Time-course of recovery from adaptation by hydroxyproline-sensitive lobster olfactory receptor neurons *Biol. Bull.* **187** 259–60

Gomez G and Atema J 1996a Temporal resolution in olfaction: II. Time course of recovery from adaptation in lobster chemoreceptor cells *J. Neurophysiol.* **76** 1340–3

Gomez G and Atema J 1996b Temporal resolution in olfaction: stimulus integration time of lobster chemoreceptor cells *J. Exp. Biol.* **199** 1771–9

Gomez G, Voigt R and Atema J 1994 Frequency filter properties of lobster chemoreceptor cells determined with high-resolution stimulus measurement *J. Comp. Physiol.* A **174** 803–11

Gomez G, Voigt R and Atema J 1999 Temporal resolution in olfaction: III. Flicker fusion and concentration-dependent synchronization with stimulus pulse trains of antennular chemoreceptor cells in the American lobster *J. Comp. Physiol.* A **185** 427–36

Grasso F W and Basil J A 2002 How lobsters, crayfishes, and crabs locate sources of odor: current perspectives and future directions *Curr. Opin. Neurobiol.* **12** 721–7

Grunert U and Ache B W 1988 Ultrastructure of the aesthetasc (olfactory) sensilla of the spiny lobster *Panulirus argus Cell Tissue Res.* **251** 95–103

Hallberg E, Johansson K U I and Elofsson R 1992 The aesthetasc concept—structural variations of putative olfactory receptor cell complexes in crustacea *Microsc. Res. Tech.* **22** 325–35

Han T, Yang K S and Lee K 2010 Heat transfer characterization of two isothermal circular cylinders in proximity *J. Heat Transfer* **132** 034504

Hatt H and Ache B W 1996 Patch-clamping arthropod olfactory receptor neurons to study mechanisms of olfactory transduction *J. Neurosci. Methods* **69** 43–9

Hines E L, Llobet E and Gardner J W 1999 Electronic noses: a review of signal processing techniques *IEE Proc. Circuits Devices Syst.* **146** 297–310

Hood D C and Grover B G 1974 Temporal summation of light by a vertebrate visual receptor *Science* **184** 1003–5

Horner A J, Weissburg M J and Derby C D 2004 Dual antennular chemosensory pathways can mediate orientation by Caribbean spiny lobsters in naturalistic flow conditions *J. Exp. Biol.* **207** 3785–96

Ishida H and Moriizumi T 2004 *Machine Olfaction for Mobile Robots* (Weinheim: Wiley-VCH) pp 399–417

Ishida H, Nakayama G, Nakamoto T and Moriizumi T 2005 Controlling a gas/odor plume-tracking robot based on transient responses of gas sensors *IEEE Sensors J.* **5** 537–45

James D, Scott S M, Ali Z and O'Hare W T 2005 Chemical sensors for electronic nose systems *Microchim. Acta* **149** 1–17

Juncu G 2008 Conjugate heat/mass transfer from a circular cylinder with an internal heat/mass source in laminar crossflow at low Reynolds numbers *Int. J. Heat Mass Transfer* **51** 3255–6

Junek S, Kludt E, Wolf F and Schild D 2010 Olfactory coding with patterns of response latencies *Neuron* **67** 872–84

Kaissling K E 1998 Flux detectors versus concentration detectors: two types of chemoreceptors *Chem. Senses* **23** 99–111

Keller T A, Powell I and Weissburg M J 2003 Role of olfactory appendages in chemically mediated orientation of blue crabs *Marine Ecol.—Prog. Ser.* **261** 217–31

Keller T A and Weissburg M J 2004 Effects of odor flux and pulse rate on chemosensory tracking in turbulent odor plumes by the blue crab *Callinectes sapidus Biol. Bull.* **207** 44–55

Kikas T, Ishida H, Webster D R and Janata J 2001a Chemical plume tracking: 1. Chemical information encoding *Anal. Chem.* **73** 3662–8

Kikas T, Janata P, Ishida H and Janata J 2001b Chemical plume tracking: 2. Multiple-frequency modulation *Anal. Chem.* **73** 3669–73

Kirsch V 2007 Stokes flow in model fibrous filters *Separation Purif. Technol.* **58** 288–94

Koehl M A R 1992 Hairy little legs: feeding, smelling, and swimming at low Reynolds number. Fluid dynamics in biology *Contemp. Math.* **141** 33–64

Koehl M A R 1995 Fluid flow through hair-bearing appendages: feeding, smelling, and swimming at low and intermediate Reynolds number *Biological Fluid Dynamics (Society of Experimental Biology Symposium* vol 49*)* ed C Ellington and T J Pedley pp 157–182

Koehl M A R 1996 Small-scale fluid dynamics of olfactory antennae *Mar. Freshwater Behav. Physiol.* **27** 127–41

Koehl M A R 2001a Fluid dynamics of animal appendages that capture molecules: arthropod olfactory antennae *IMA Workshop on Computational Modeling in Biological Fluid Dynamics* pp 97–116

Koehl M A R 2001b Transitions in function at low Reynolds number: hair-bearing animal appendages *Math. Methods Appl. Sci.* **24** 1523–32
Koehl M A R 2004 Biomechanics of microscopic appendages: functional shifts caused by changes in speed *J. Biomech.* **37** 789–95
Koehl M A R 2006 The fluid mechanics of arthropod sniffing in turbulent odor plumes *Chem. Senses* **31** 93–105
Koehl M A R, Koseff J R, Crimaldi J P, McCay M G, Cooper T, Wiley M B and Moore P A 2001 Lobster sniffing: antennule design and hydrodynamic filtering of information in an odor plume *Science* **294** 1948–51
Lange C F, Durst F and Breuer M 1998 Momentum and heat transfer from cylinders in laminar crossflow at $10(-4) <= \mathrm{Re} <= 200$ *Int. J. Heat Mass Transfer* **41** 3409–30
Laverack M S 1988 *Sensory Biology of Aquatic Animals* ed J Atema (New York: Springer) pp 287–317
Liao Q and Cowen E A 2002 The information content of a scalar plume—a plume tracing perspective *Environ. Fluid Mech.* **2** 9–34
Loudon C, Best B A and Koehl M A R 1994 When does motion relative to neighboring surfaces alter the flow-through arrays of hairs *J. Exp. Biol.* **193** 233–54
Loudon C and Koehl M A R 2000 Sniffing by a silkworm moth: wing fanning enhances air penetration through and pheromone interception by antennae *J. Exp. Biol.* **203** 2977–90
Mead K S and Koehl M A R 2000 Stomatopod antennule design: the asymmetry, sampling efficiency and ontogeny of olfactory flicking *J. Exp. Biol.* **203** 3795–808
Mead K S, Koehl M A R and O'Donnell M J 1999 Stomatopod sniffing: the scaling of chemosensory sensillae and flicking behavior with body size *J. Exp. Marine Biol. Ecol.* **241** 235–61
Mead K S and Weatherby T M 2002 Morphology of stomatopod chemosensory sensilla facilitates fluid sampling *Invert. Biol.* **121** 148–57
Mead K S, Wiley M B, Koehl M A R and Koseff J R 2003 Fine-scale patterns of odor encounter by the antennules of mantis shrimp tracking turbulent plumes in wave-affected and unidirectional flow *J. Exp. Biol.* **206** 181–93
Michel W C and Ache B W 1994 Odor-evoked inhibition in primary olfactory receptor neurons *Chem. Senses* **19** 11–24
Moore P A and Atema J 1991 Spatial information in the 3-dimensional fine-structure of an aquatic odor plume *Biol. Bull.* **181** 408–18
Moore P A, Atema J and Gerhardt G A 1991 Fluid-dynamics and microscale chemical movement in the chemosensory appendages of the lobster *Homarus americanus Chem. Senses* **16** 663–74
Moore P A, Scholz N and Atema J 1991 Chemical orientation of lobsters *Homarus americanus* in turbulent odor plumes *J. Chem. Ecol.* **17** 1293–307
Moore P A, Zimmer-Faust R K, Bement S L, Weissburg M J, Parrish J M and Gerhardt G A 1992 Measurement of microscale patchiness in a turbulent aquatic odor plume using a semiconductor-based microprobe *Biol. Bull.* **183** 138–42
Moore P and Crimaldi J 2004 Odor landscapes and animal behavior: tracking odor plumes in different physical worlds *J. Mar. Syst.* **49** 55–64
Nakamoto T and Ishida H 2008 Chemical sensing in spatial/temporal domains *Chem. Rev.* **108** 680–704
Page J L, Dickman B D, Webster D R and Weissburg M J 2011a Getting ahead: context-dependent responses to odorant filaments drive along-stream progress during odor tracking in blue crabs *J. Exp. Biol.* **214** 1498–512
Page J L, Dickman B D, Webster D R and Weissburg M J 2011b Staying the course: chemical signal spatial properties and concentration mediate cross-stream motion in turbulent plumes *J. Exp. Biol.* **214** 1513–22
Reidenbach M A, George N and Koehl M A R 2008 Antennule morphology and flicking kinematics facilitate odor sampling by the spiny lobster *Panulirus argus J. Exp. Biol.* **211** 2849–58
Rospars J P, Krivan V and Lansky P 2000 Perireceptor and receptor events in olfaction. comparison of concentration and flux detectors: a modeling study *Chem. Senses* **25** 293–311
Rubenstein D I and Koehl M A R 1977 Mechanisms of filter feeding—some theoretical considerations *Am. Nat.* **111** 981–94
Settles G S 2005 Sniffers: fluid-dynamic sampling for olfactory trace detection in nature and homeland security—The 2004 Freeman Scholar Lecture *J. Fluids Eng.—Trans. ASME* **127** 189–218
Spencer M and Linberg K A 1986 Ultrastructure of aesthetasc innervation and external morphology of the lateral antennule setae of the spiny lobster *Panulirus interruptus* (Randall) *Cell Tissue Res.* **245** 69–80
Spors H, Wachowiak M, Cohen L B and Friedrich R W 2006 Temporal dynamics and latency patterns of receptor neuron input to the olfactory bulb *J. Neurosci.* **26** 1247–59
Stacey M T, Mead K S and Koehl M A R 2002 Molecule capture by olfactory antennules: mantis shrimp *J. Math. Biol.* **44** 1–30
Stanescu G, Fowler A J and Bejan A 1996 The optimal spacing of cylinders in free-stream cross-flow forced convection *Int. J. Heat Mass Transfer* **39** 311–7
Su C Y, Martelli C, Emonet T and Carlson J R 2011 Temporal coding of odor mixtures in an olfactory receptor neuron *Proc. Natl Acad. Sci. USA* **108** 5075–80
Tamada K and Fujikawa H 1959 The steady flow of viscous fluid at low Reynolds numbers passing obliquely through a plane grid made of equal parallel circular cylinders *J. Phys. Soc. Japan* **14** 202–16
Trapidorosenthal H G, Carr W E S and Gleeson R A 1987 Biochemistry of an olfactory purinergic system—dephosphorylation of excitatory nucleotides and uptake of adenosine *J. Neurochem.* **49** 1174–82
Vlasov Y, Ermolenko Y, Legin A, Rudnitskaya A and Kolodnikov V 2010 Chemical sensors and their systems *J. Anal. Chem.* **65** 880–98
Wang M and Georgiadis J G 1996 Conjugate forced convection in crossflow over a cylinder array with volumetric heating *Int. J. Heat Mass Trans.* **39** 1351–61
Webster D R, Rahman S and Dasi L P 2001 On the usefulness of bilateral comparison to tracking turbulent chemical odor plumes *Limnol. Oceanogr.* **46** 1048–53
Webster D R, Rahman S and Dasi L P 2003 Laser-induced fluorescence measurements of a turbulent plume *ASCE J. Eng. Mech.* **129** 1130–7
Webster D R and Weissburg M J 2001 Chemosensory guidance cues in a turbulent chemical odor plume *Limnol. Oceanogr.* **46** 1034–47
Webster D and Weissburg M J 2009 The hydrodynamics of chemical cues among aquatic organisms *Annu. Rev. Fluid Mech.* **41** 73–90
Weissburg M J and Zimmer-Faust R K 1993 Life and death in moving fluids—hydrodynamic effects on chemosensory-mediated predation *Ecology* **74** 1428–43
Yoo S Y, Kwon H K and Kim J H 2007 A study on heat transfer characteristics for staggered tube banks in cross-flow *J. Mech. Sci. Technol.* **21** 505–12
Young W R and Jones S 1991 Shear dispersion *Phys. Fluids A Fluid Dyn.* **3** 1087–101
Zettler E and Atema J 1999 Chemoreceptor cells as concentration slope detectors: preliminary evidence from the lobster nose *Biol. Bull.* **197** 252–3
Zimmer-Faust R K, Finelli C M, Pentcheff N D and Wethey D S 1995 Odor plumes and animal navigation in turbulent water-flow—a field-study *Biol. Bull.* **188** 111–6